Self-Reporting Hypoxia-Responsive Supramolecular Phototheranostic Nanomaterials Based on AIEgen and Azocalixarene

Xiao-Wen Han,[†] Guo-Ling Zhang,[†] Pu Chen,[†] Jing Zhang,[†] Guogang Shan,[§] Chunxuan Qi,[†] Ben Zhong Tang[‡,*] and Hai-Tao Feng,[†,*]

[†]AIE Research Center, Shaanxi Key Laboratory of Phytochemistry, College of Chemistry and Chemical Engineering, Baoji University of Arts and Sciences, Baoji 721013, China

[‡]School of Science and Engineering, Shenzhen Institute of Aggregate Science and Technology, The Chinese University of Hong Kong, Shenzhen (CUHK-Shenzhen), Shenzhen 518172, China

[§]National & Local United Engineering Laboratory for Power Batteries, Department of Chemistry, Northeast Normal University, Changchun 130024, China

KEYWORDS: aggregation-induced emission, host-guest interaction, photodynamic therapy, hypoxia, bioimaging

ABSTRACT: Hypoxia is a significant feature in most of solid tumors and developing hypoxia-responsive phototheranostic system is still a challenge. In this contribution, a supramolecular assembly strategy based on sulfonate-functionalized azocalix[4]arene (SAC4A) and cationic aggregation-induced emission photosensitizer (namely TPA-H) was proposed for hypoxia-responsive bioimaging and photodynamic therapy (PDT). Upon supramolecular complexation of TPA-H and SAC4A through electrostatic interaction, the fluorescence and reactive oxygen species (ROS) generation of TPA-H were largely inhibited. In hypoxic tumors, the azo group of SAC4A can be reduced to aniline derivative and release the included TPA-H to recover its pristine fluorescence and ROS. Interestingly, the free TPA-H undergoes cell membrane-to-mitochondria translocation during cell imaging, achieving a real-time self-reporting PDT system. In vivo tumor imaging and therapy reveal that this as-prepared supramolecular complexes have good biosafety and efficient antitumor activity under hypoxia. Such hypoxia-responsive supramolecular photosensitizer system will enrich image-guided PDT.

INTRODUCTION

Photodynamic therapy (PDT) as a burgeoning non-invasive therapeutic method has been utilized in preclinical treatment thanks to its easy accessibility, low toxicity, high spatiotemporal precision, and less incidence to evolve drug resistance.[1-5] Photosensitizer (PS) is the primary element of PDT, which can generate two kinds of reactive oxygen species (ROS) upon photoexcitation to ablate cancer cells.[6-8] One is type I ROS depending less on oxygen, such as hydroxyl radical ($OH^{\bullet}$), superoxide radical ($O_2^{\bullet-}$) and hydrogen peroxide (H_2O_2), which shows great potential for antitumor treatment under hypoxia.[9,10] The other is type II ROS including singlet oxygen ($^1O_2$). Besides the efficient therapy capability, fluorescence photosensitizers can visualize the tumor locations and image organelles in cancer cells as well. Thus, image-guided PDT is a versatile theranostic technique. While, the "always on" mode of photosensitizers contributes to a low target-to-background ratio on account of a high background interference.[11,12] Therefore, development of "off-on" photosensitizer system with high sensitivity to tumor microenvironment change is extremely desirable to detect cancer in the initial phase.

Hypoxia is a significant feature of most solid tumors, which is stemmed from the imbalance between the enhanced oxygen depletion caused by the fast proliferation of tumor cells and an insufficient oxygen supply arisen arising from limited neovascularization.[13-20] Hypoxia is also associated with tumor invasion, metastasis, increased resistance to radiotherapy and chemotherapy.[21,22] Moreover, hypoxic tumors generally display much stronger reducibility than those normoxic cells due to the overexpression of reductases, such as nitro-reductase, azo-reductase, glutathione, NAD(P)H: quinone oxidoreductase 1 and so on.[23-27] By virtue of the intense reductive ability, numerous hypoxia responsive probes have been created.[28-30] Among these, azobenzene derivatives are a kind of classical hypoxia-sensitive probes, which can be reduced to amine derivatives by breaking the azo group using azo-reductase in hypoxic microenvironment.[31-35] Usually, azo-based luminophores emit weak fluorescence upon excitation owing to the excited energy consumption by rapid intramolecular rotation around the N=N double bond.[36-38] After reduction of the azo group, intense fluorescence is attained that is the design principle for hypoxia-responsive probes. To now, many hypoxia-sensitive probes have been constructed by azo reduction strategy through using a single molecule system. For example, Nagano and co-workers reported a series of azo-containing probes composed of a NIR cyanine fluorophore and a fluorescence quencher moiety at two ends of azo group showing high sensitivity to hypoxia.[33,39] However, these traditional fluorescence probes after

dissociation always encounter aggregation-caused quenching (ACQ) effect in the aggregated state or physiological environment, which largely reduces the ROS generation efficiency and fluorescence quantum yield (QY).[40] Moreover, the direct covalent linking strategy also confronts complicated synthesis and limited activity adjustment.

The emerging aggregation-induced emission luminogens (AIEgens) with high QY, good photostability and efficient ROS generation in the aggregated state are ideal candidates to construct chemo/bioprobes.[41-49] While, AIEgens emitting bright fluorescence upon aggregation can cause large background noise during bio-imaging. To fulfill the whole potential of AIE photosensitizers and smartly tune their photophysical properties, a noncovalent strategy based on the host–guest interaction is proposed. In contrast to single molecule systems, supramolecular interactions can be facilely operated and extensively used for high throughput screening.[50-52] Organic macrocycles as the main host compounds are essential ingredients in supramolecular assembly, which can selectively include guest molecules in their inherent cavities to form complexes.[53-55] Among them, calixarene affording a cone conformation is well-known for easy alteration, good compatibility, and multiple responses to stimuli.[56,57] Now, calixarene derivatives have been widely utilized for biomedical materials in bio-imaging, drug delivery, and therapeutic agents.[58-61] For example, Guo reported several calixarene-based supramolecular fluorescence probes for hypoxia imaging but without deeply exploring their antitumor capability.[62,63]

Herein, we develop a supramolecular assembly strategy based on sulfonate-functionalized azocalix[4]arene (SAC4A) and red-emitting AIEgen for hypoxia-responsive bioimaging and photodynamic therapy. In this system, cationic AIEgen composed of triphenylamine and quaternary ammonium salt (namely TPA-H) can be encapsulated in the cavity of azocalix[4]arene through electrostatic interaction (Scheme 1A). The as-prepared supramolecular complexes result in a quenched fluorescence. When exposing the complexes under hypoxia, the azo group is reduced to aniline derivative and released the included AIEgen, recovering its pristine fluorescence for cell imaging. Interestingly, the dissociative TPA-H undergoes cell membrane-to-mitochondria translocation during fluorescence imaging, constructing a real-time self-reporting system to monitor the PDT process *in situ* (Scheme 1B). Moreover, TPA-H can generate efficient singlet oxygen ($^1O_2$) and superoxide radical anions ($O_2^{\bullet-}$) under light excitation for PDT with good performance. In vivo hypoxia-responsive tumor imaging and therapy manifest that our supramolecular complexes have good biosafety and efficient antitumor efficacy. It is predicted that such host−guest strategy avoids complicated molecular synthesis and paves a way for efficient image-guided PDT.

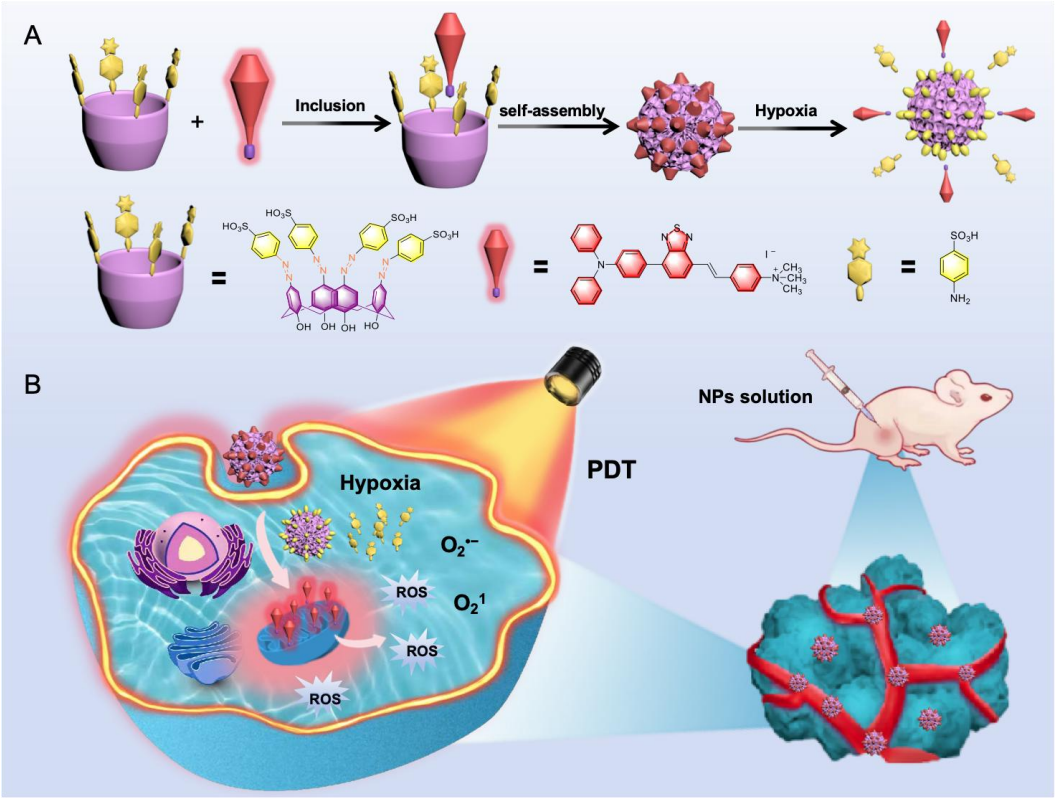

Scheme 1. (A) Schematic illustration of hypoxia-responsive supramolecular assembly strategy, in which the fluorescence of TPA-H is quenched by complexation with SAC4A in aqueous solution but restored by the breaking of azo bonds in a hypoxic environment. (B) Graphical diagram of cell imaging and photodynamic therapy of TPA-H ⊂ SAC4A complexes under hypoxia.

RESULTS AND DISCUSSION

During supramolecular assembly, the positive photosensitizer should be pre-included in the cavity of SAC4A through charge-aided hydrogen-bonding interaction. Then, upon encountering hypoxic microenvironment, the as-obtained supramolecular complexes dissociated by reduction of azo group are essential to release the photosensitizer. Negative sulfonate groups decorated at the para-position of azobenzene are aimed to give a water-soluble calixarene and provide

electrostatic interaction with positive AIEgen. The cone-shaped SAC4A has a big 3D cavity that is large enough to encapsulate TPA-H. Therefore, our hypoxia-responsive host-guest assembly strategy is feasible theoretically. The detailed synthetic routes of TPA-H and SAC4A are presented in Scheme S1-S2. Their molecular structures were characterized by ^{1}H and ^{13}C NMR and high-resolution mass spectrometry (HRMS) (Figure S1-S8, Supporting Information).

The photophysical properties of TPA-H and its supramolecular assemblies were first evaluated by ultraviolet–visible (UV–vis) absorption and photoluminescence (PL) spectra. As illustrated in Figure 1A, a main absorption profile of TPA-H is observed at 465 nm and its maximum PL band centers at 654 nm in pure dimethylsulfoxide (DMSO) solution. AIE behaviors of TPA-H were investigated in DMSO and dichloromethane (DCM) mixtures. TPA-H emitted weak red fluorescence in DMSO. When adding poor solvent DCM to the solution gradually, increased fluorescence was observed accompanied by some hypsochromic shift in PL spectra due to twisted intramolecular charge transfer (Figure S9). Above results demonstrated TPA-H is AIE-active. Then, theoretical calculations were carried out to optimize its molecular structure and orbital by using density functional theory (DFT) methods (Figure 1B). The whole molecule adopted a twisted conformation due to introduction of triphenylamine unit, which is favorable for efficient emission in the aggregated state. The highest occupied molecular orbital (HOMO) of TPA-H mainly located on the triphenylamine moiety, while the lowest unoccupied molecular orbital (LUMO) concentrated on the diazosulfide and phenyl rings. The energy gap was computed to be 1.90 eV. In addition, the lowest energy gap of singlet and triplet states ($\Delta E_{S1\text{-}T2}$) of TPE-H was computed to be 0.06 eV, which is favorable to promote intersystem crossing (ISC) to triplet state. TPA-H fluoresced brightly with a QY of 9.0% in aqueous medium. Upon addition of 2.0 equivalents (eq.) of SAC4A, the fluorescence intensity dramatically decreased with a QY of 0.85%, implying strong electrostatic interactions (Figure 1C). Therefore, it is anticipated that TPA-H and SAC4A formed supramolecular complexes (TPA-H⊂SAC4A). PL titration was carried out to further verify the host-guest assembly. With enhancing the concentration of SAC4A, the fluorescence intensity of TPA-H gradually reduced and achieved equilibrium until 2.0 equivalents of SAC4A was added (Figure S10). After supramolecular assembly of SAC4A and TPA-H, the zeta potential of the resultant nanoparticles changed from ~15.0 mV for TPA-H to ~−26.4 mV for TPA-H⊂SAC4A due to the negative charges of sulfonate motif in SAC4A (Figure 1D). Additionally, the time-resolved fluorescence decay curves of TPA-H and its supramolecular complexes were tested. TPA-H showed a lifetime of 1.78 and 1.90 ns in DMSO solution and powders, respectively. After self-assembly with SAC4A in aqueous solution, the lifetime of TPA-H⊂SAC4A decreased to 1.22 ns (Figure 1E and 1F). Dynamic light scattering (DLS) data showed that TPA-H formed micro-assemblies with a mean diameter of about 1554 nm in water solution (Figure 1G). After complexation with SAC4A, the aggregate size decreased to 243 nm owing to dissolution enhancement by water soluble of SAC4A (Figure 1F). Then, the photostability of supramolecular nanomaterials was evaluated under different times, different pH values and various species like HPO_4^-, CO_3^-, Mg^{2+}, Na^+, Cu^{2+}, K^+, Ca^{2+}, they all showed little influence on their PL properties (Figure S11).

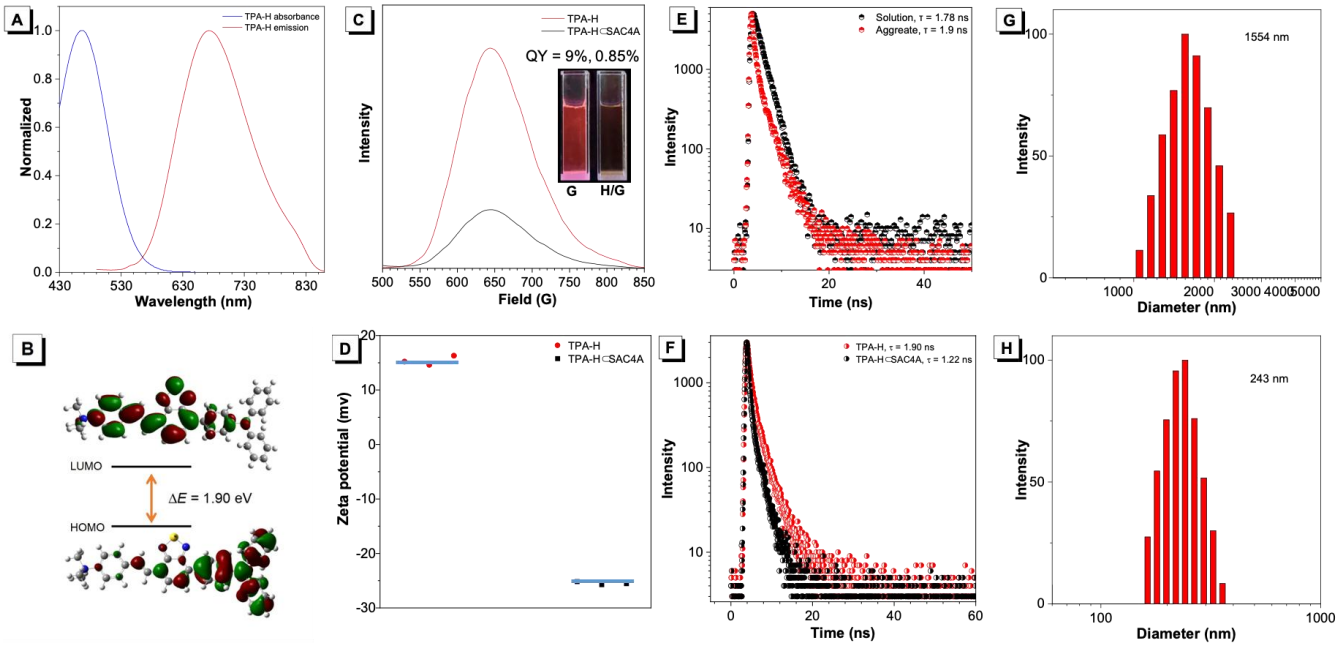

Figure 1. (A) Normalized absorption spectra and PL spectra of TPA-H in DMSO solution. [TPA-H] = [SAC4A] =10 μM. (B) Molecular orbital and geometry optimizations of TPA-H. (C) PL titration of TPA-H in the presence of 0 and 2.0 equivalents of SAC4A in aqueous medium. Inset: Images of TPA-H and TPA-H⊂SAC4A taken under 365 nm UV irradiation in aqueous medium. Excitation wavelength: 480 nm. [TPA-H] =10 μM. (D) The zeta potential of TPA-H and TPA-H⊂SAC4A in water. [TPA-H] = [SAC4A] =10 μM. (E) Time-resolved fluorescence decay curves of TPA-H in DMSO solution and powders. [TPA-H] =10 μM. (F) Time-resolved fluorescence decay

curves of TPA-H and TPA-H⊂SAC4A in water. [TPA-H] = [SAC4A] =10 μM. Dynamic light scattering diagram of TPA-H (G) and TPA-H⊂SAC4A (H) in aqueous medium. [TPA-H] = [SAC4A] =10 μM.

To explore the potential self-assembly mechanism, 2D COSY NMR, ^{1}H NMR titrations, and 2D NOESY NMR of TPA-H with SAC4A were implemented in d_6-DMSO. Through analysis of 2D COSY NMR, their specific protons are clearly characterized (Figure S12-S14). When adding 0 to 2.0 equivalents of SAC4A to TPA-H, the signal of the methyl proton (Ha), phenyl ring protons (Hb and Hc) and vinyl double bonds (Hd and He) of TPE-H presented evident upfield-shifts by δ −0.036, −0.035, −0.031, −0.019 and −0.018 ppm (Figure S15 and Table S1) showing effective shielding effect by the aromatic rings of SAC4A. It was properly inferred that the quaternary ammonium moiety was inserted in the cavity of SAC4A. The protons of triphenylamine and diazosulfide unit showed minor change, implying these segments kept away from the cavity. Due to the inclusion of TPA-H, the phenyl ring proton Hf and Hg of SAC4A gave an obvious downfield shift by δ 0.015 and 0.011 ppm (Figure S16). The 2D NOESY spectrum of mixture of TPA-H and SAC4A showed an obvious NOE signal between vinyl proton (He) of TPA-H and phenyl proton (Hf) of SAC4A, indicating that TPA-H is partially inserted in the cavity of SAC4A (Figure S17). Sodium dithionite ($Na_2S_2O_4$) as a reducing reagent was selected to verify the reduction of azo group in SAC4A by using HRMS spectroscopy. Upon addition of $Na_2S_2O_4$ to SAC4A solution, the N=N double bond rapidly decomposed to form *p*-aminocalix[4]arene (Figure 2A and 2B). Then, the reaction between TPA-H⊂SAC4A and sodium dithionite was studied by using UV and PL spectroscopy. As shown in Figure 2C, the UV intensity was evidently increased after complexation with SAC4A in aqueous medium. When sodium dithionite was added in the complex of TPA-H⊂SAC4A, the absorption band of the mixture showed a similar profile with TPA-H. Meanwhile, the red fluorescence at 654 nm was turned on gradually over time (Figure 2D). Above data supported our hypothesis that azo group of SAC4A was broken to release the included TPA-H and emit bright fluorescence, which further stimulates us to study their hypoxia-responsive bioimaging. The HeLa cells were incubated in normoxic (20% O_2) and hypoxic (less than 0.1% O_2) conditions with the same concentration of TPA-H⊂SAC4A nanomaterials. Figure 2E and Figure S18 revealed that the fluorescence intensity enhanced more than 2-fold in hypoxia than that in normal oxygen concentration. This indicated that SAC4A is decomposed in hypoxic microenvironment and released TPA-H from its cavity.

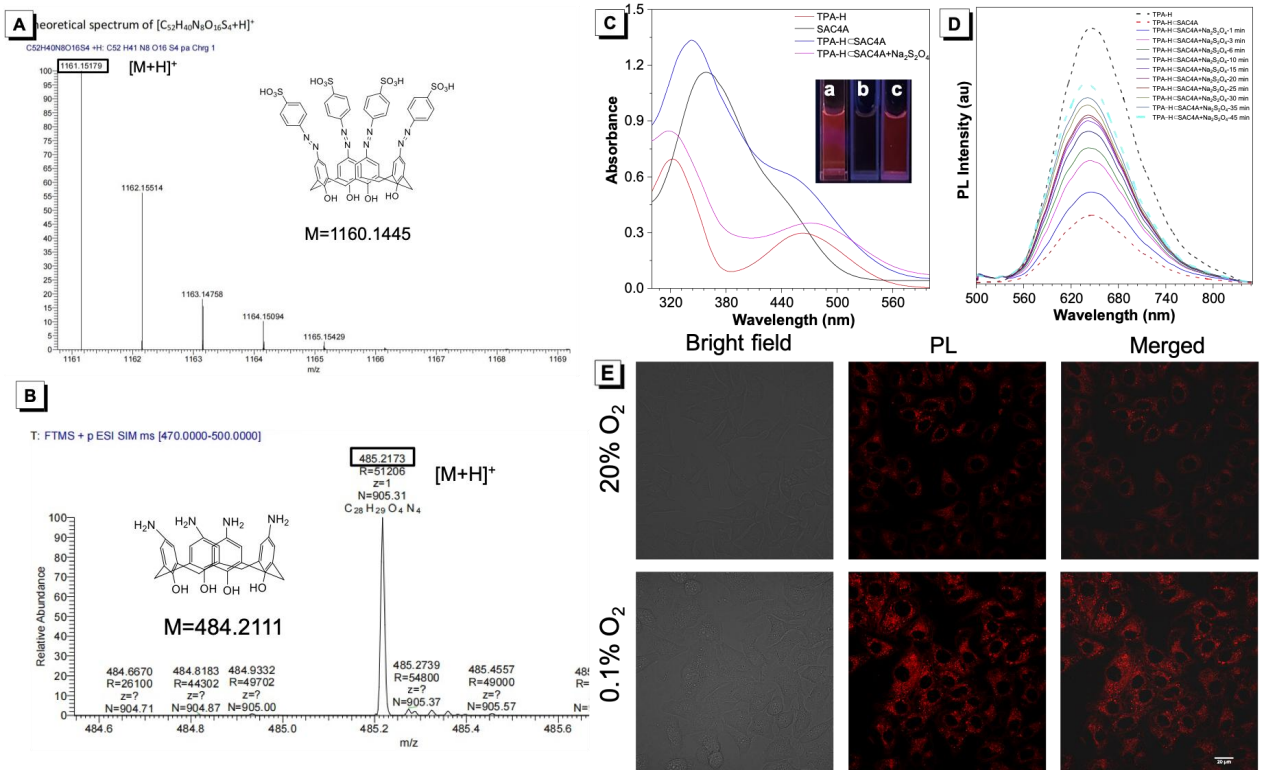

Figure 2. HRMS spectra of SAC4A before (A) and after (B) the incubation with $Na_2S_2O_4$. (C) Absorption spectra of TPA-H reacting with $Na_2S_2O_4$ and SAC4A in aqueous medium, [TPA-H] = [SAC4A] =20 μM, [$Na_2S_2O_4$] = 100 mM. Inset: Fluorescence images of TPA-H (a), TPA-H⊂SAC4A (b) and TPA-H⊂SAC4A + $Na_2S_2O_4$ (c) taken under 365 nm UV irradiation in aqueous medium. (D) PL spectra of TPA-H and TPA-H⊂SAC4A with $Na_2S_2O_4$ at different reacting time in aqueous medium. Excitation wavelength: 480 nm. [TPA-H] = [SAC4A] =10 μM, [$Na_2S_2O_4$] = 50 mM. (E) Confocal laser scanning microscopy images of HeLa cells incubated with TPA-H⊂SAC4A under hypoxic (less than 0.1% O_2) or normoxic (20% O_2) conditions for 12 h. [TPA-H] = [SAC4A] = 10 μM, Ex = 561 nm, Em = 600–700 nm. Scale bar = 20 μm.

ROS generation efficiency is a key factor to evaluate the PDT ability. The whole ROS capability was assessed by indicator 2,7-dichlorodihydrofluorescein (DCFH-DA) under white light. DCFH-DA was weakly emissive under light irradiation (Figure 3A and Figure S19). While, its fluorescence intensity was drastically increased with a 54-fold enhancement after illuminating for 6 s, proving a rapid and high ROS generation efficiency. After complexation with SAC4A, the ROS generation efficiency was largely suppressed. To determine the species of ROS, 9,10-anthracenediyl-bis(methylene)-dimalonic acid (ABDA) was utilized to detect type II ROS $^1O_2$ through using absorption spectra. As shown in Figure 3B and Figure S20, ABDA was almost no change upon exposure to white light. While, upon addition of TPA-H, a large decrease in the absorption profile was observed with a 91% of ABDA consumption. Interestingly, the supramolecular complexes TPA-H⊂SAC4A totally inhibited the $^1O_2$ generation. Then, we verified that if TPA-H can produce type I ROS, dihydrorhodamine 123 (DHR123) was first selected as radical ROS indicator to monitor $O_2^{\bullet-}$. From the PL spectra we can see that DHR123 was almost unchanged under illumination (Figure 3C and Figure S21). However, the mixture of DHR123 and TPA-H showed a sharp enhancement in PL intensity. After host-guest interaction with SAC4A, the $O_2^{\bullet-}$ generation efficiency largely decreased. In addition, type I ROS species were also explored by electron spin resonance (ESR) spectra using 4-amino-2,2,6,6-tetramethylpiperidine (TEMP) and 5,5-dimethyl-1-pyrroline-*N*-oxide (DMPO) as spin-trap probes for $^1O_2$ and free radicals, respectively. Compared with the dark state, TPA-H presented strong $^1O_2$ generation (Figure 3D), and no ESR signals were attained in TPA-H⊂SAC4A system, which is coincident with absorption data. Moreover, TPA-H and its supramolecular assemblies showed evident $O_2^{\bullet-}$ signals after interaction with DMPO in methanol (Figure 3E) and no obvious OH• radical response was observed in water (Figure 3F). Thus, such results indicated that TPE-H can efficiently generate $^1O_2$ and $O_2^{\bullet-}$ ROS. While, SAC4A can largely restrain $^1O_2$ generation after interaction with TPA-H. Then, DCFH-DA was used to detect intracellular ROS generation (Figure S22). After treating with DCFH-DA and TPA-H, bright green fluorescence was observed in HeLa cells under light excitation, while no fluorescence was detected in the dark state and DCFH-DA group, implying that TPA-H can produce ROS under light illumination in living cells.

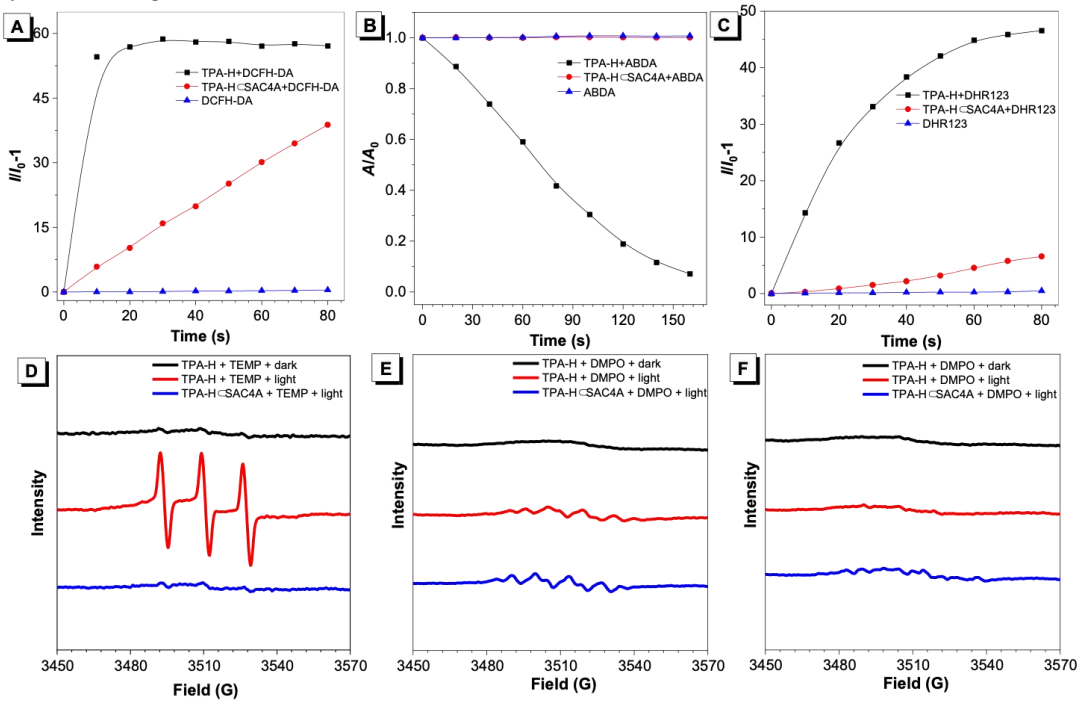

Figure 3. (A) Relative changes in fluorescence intensity (I/I_0-1) at 525 nm of DCFH-DA and mixtures of DCFH-DA with TPA-H and TPA-H⊂SAC4A in PBS under white light with different irradiation time. (B) Relative changes in absorbance of ABDA in the presence of TPA-H and TPA-H⊂SAC4A upon white light irradiation for different time, where A_0 and A are the absorbance of ABDA at 378 nm before and after irradiation. (C) Relative change in fluorescence intensity (I/I_0-1) at 526 nm of DHR123, mixtures of DHR123 with TPA-H and TPA-H⊂SAC4A in PBS upon white light irradiation for different time. [DCFH-DA] = 5 μM, [ABDA] = 50 μM, [TPA-H] = [SAC4A] = [DCFH-DA] = [DHR-123] = 10 μM. Light power: 100 mW cm^{-2}. (D–F) ESR signals of DMPO and TEMP for characterization of $^1O_2$, $O_2^{\bullet-}$ and OH• in the presence of TPA-H (1 μM) and TPA-H⊂SAC4A (1 μM) upon white light irradiation. TPA-H exhibited remarkable $^1O_2$ radical signals after interaction with TEMP in water (D), exhibits a small amount of $O_2^{\bullet-}$ radical signaling after interaction with DMPO in methanol (E) and no OH• radical signaling after interaction with DMPO in water (F). TPA-H⊂SAC4A exhibits obvious $O_2^{\bullet-}$ radical signaling (E) after interaction with DMPO in methanol and no $^1O_2$ (D) and OH• (F) radical response in water. Light power: 100 mW cm^{-2}.

Then, the cytotoxicity of TPA-H was assessed by CCK-8 assay in HeLa cells. As illustrated in Figure 4A, the viability of HeLa cells is higher than 80% after incubation in 10 μM of TPA-H for 24 h under dark state, implying their good biocompatibility. Upon the white light illuminating for 10 min, only 8.6% of cell viability remained in the presence of 10 μM of TPA-H. The photostability of TPA-H and Mito-Tracker Green were evaluated in HeLa cells (Figures 4B and Figure S23). Through continuous laser irradiation, the PL intensity of the HeLa cells stained by TPA-H presented minor change under confocal microscope after illuminating for 3 min, revealing the good photostabilities. As a control, the PL intensity of Mito-Tracker Green distinctly reduced under the same condition (Figure S23). As depicted in Figure 4C, TPA-H was used to stain HeLa cells under different incubation time. After staining with TPA-H (2 μM) for 10 min, bright red fluorescence (λ_{em} = 600-700 nm) was observed on cell membrane. Surprisingly, when extending the illumination time, TPA-H gradually migrated to other organelle in cell (Figure S24). To confirm the specific location, co-localization experiments were conducted with TPA-H and commercial Mito-tracker green (mitochondria staining dye). The red fluorescence of TPA-H was mainly located on cell membrane at the initial stage with a low Pearson's correlation coefficient (PC). Upon prolonging the incubation time to 2, 6 and 9 h, the co-localization with Mito-tracker green has an increased PC from 0.31 to 0.52 to 0.74 to 0.86, demonstrating TPA-H gradually translocated from cell membrane to mitochondria. This *in situ* real-time visualizing fluorescence migration in cells is beneficial to understand PDT process. Moreover, the live/dead cell co-staining assay further supported the PDT properties of TPA-H in the presence of Calcein-AM and propidium iodide (PI). Calcein-AM emits green fluorescence for live cells detection and PI shows red fluorescence in dead cells. When the HeLa cells were incubated with 2.5 μM of TPA-H, bright green fluorescence and slight red emission ~~was~~ were observed under light irradiation (Figure S25). Upon increasing the concentration to 10 μM, the green fluorescence totally disappeared and all cells exhibited strong red fluorescence, indicating the high PDT activity of TPA-H.

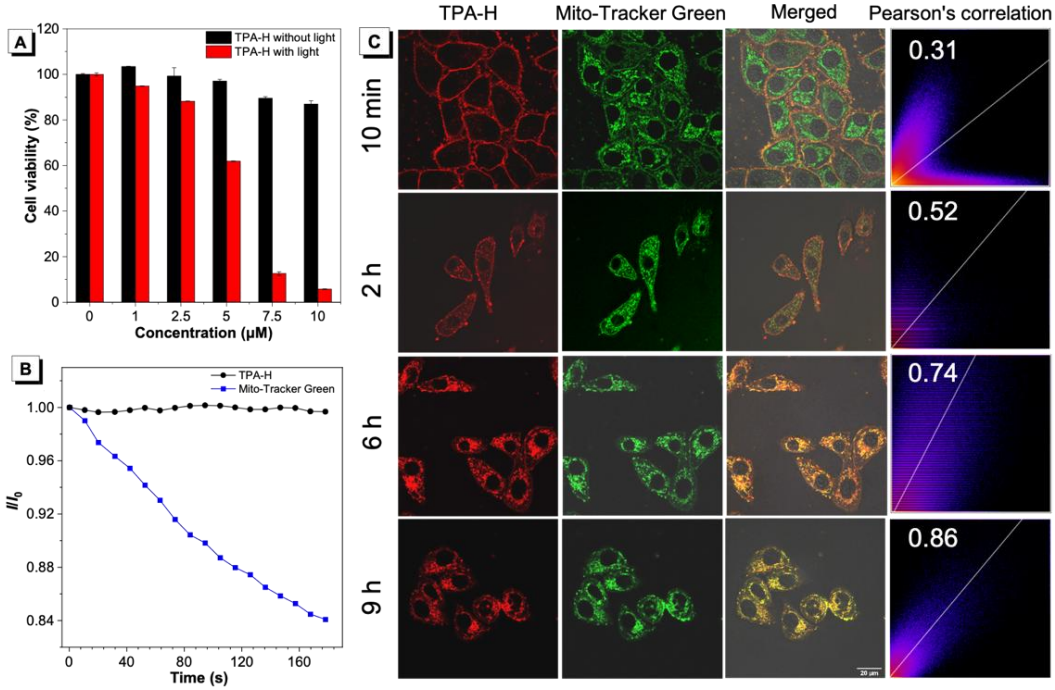

Figure 4. (A) CCK-8 assays of HeLa cells treated with various concentrations of TPA-H under dark and white light irradiation. (B) The photostability of HeLa cells treated with Mito-Tracker Green and TPA-H under continuous laser irradiation. (C) Confocal fluorescence images of HeLa cells incubated with TPA-H for various times, followed by costaining with Mito-Tracker Green for 30 min. [TPA-H] = 2 μM, Ex = 561 nm, Em = 600–700 nm; [Mito-tracker green] = 200 nM, Ex = 488 nm, Em = 500–530 nm. Scale bar = 20 μm.

We next demonstrated the PDT ability of TPA-H⊂SAC4A nanoparticles in hypoxic microenvironment. SAC4A showed good biocompatibility no matter in hypoxia or normoxia condition with/without light illumination (Figure 5A). The supramolecular assemblies also afforded high cell viability in the dark state with or without oxygen supply (Figure 5B), meaning no PDT was triggered off. When TPA-H⊂SAC4A nanoparticles were incubated in HeLa cells with normal O_2 condition under light irradiation, obvious cell killing was obtained with increasing the nanoparticle concentrations. As above-mentioned, TPA-H⊂SAC4A assemblies can drastically inhibit $^1O_2$ generation, but still produce a small quantity of $O_2^{\bullet-}$. Therefore, it can kill HeLa cells through PDT. In contrast, when they were incubated in hypoxia under illumination, the cell viability largely decreased, indicating TPA-H can be released from the cavity by decomposition of SAC4A to generate efficient ROS to ablate HeLa cells. Moreover, the live/dead cell co-staining assay was carried out to explore the PDT properties of TPA-H⊂SAC4A under hypoxia or normoxia in the presence of Calcein-AM and PI. As depicted in Figure 5C, when HeLa cells were incubated with TPA-H⊂SAC4A in normoxia condition, bright green fluorescence and small red emission were observed under light irradiation. Upon reducing O_2 concentration to 0.1%, strong red fluorescence was attained, indicating many cells were killed by PDT of TPA-H. Thus, we successfully constructed a hypoxia-responsive supramolecular phototheranostic system. In consideration of the efficient cell killing effect of TPA-H, we further explored whether TPA-H treatment will destroy the cell cycle. In this experiment, HeLa cells were treated with TPA-H for 30 min under light irradiation and then determined

by flow cytometry. It was worth noting that there occurred S phase accumulation with the increasing concentration of TPA-H (Figure 5D). In addition, CDK-2, Cyclin A2, P21 and P53 are important modulators for the cell cycle S phase. Western blot analysis manifested that TPA-H treatment resulted in CDK-2 and Cyclin A2 protein downregulation, while P21 and P53 expressions were significantly improved (Figure 5E). Of note, P21 is cyclin-dependent kinase inhibitor and P53 is tumor suppressor protein. Above results demonstrated that TPA-H may prevent HeLa cell propagation arising from cell cycle S arrest.

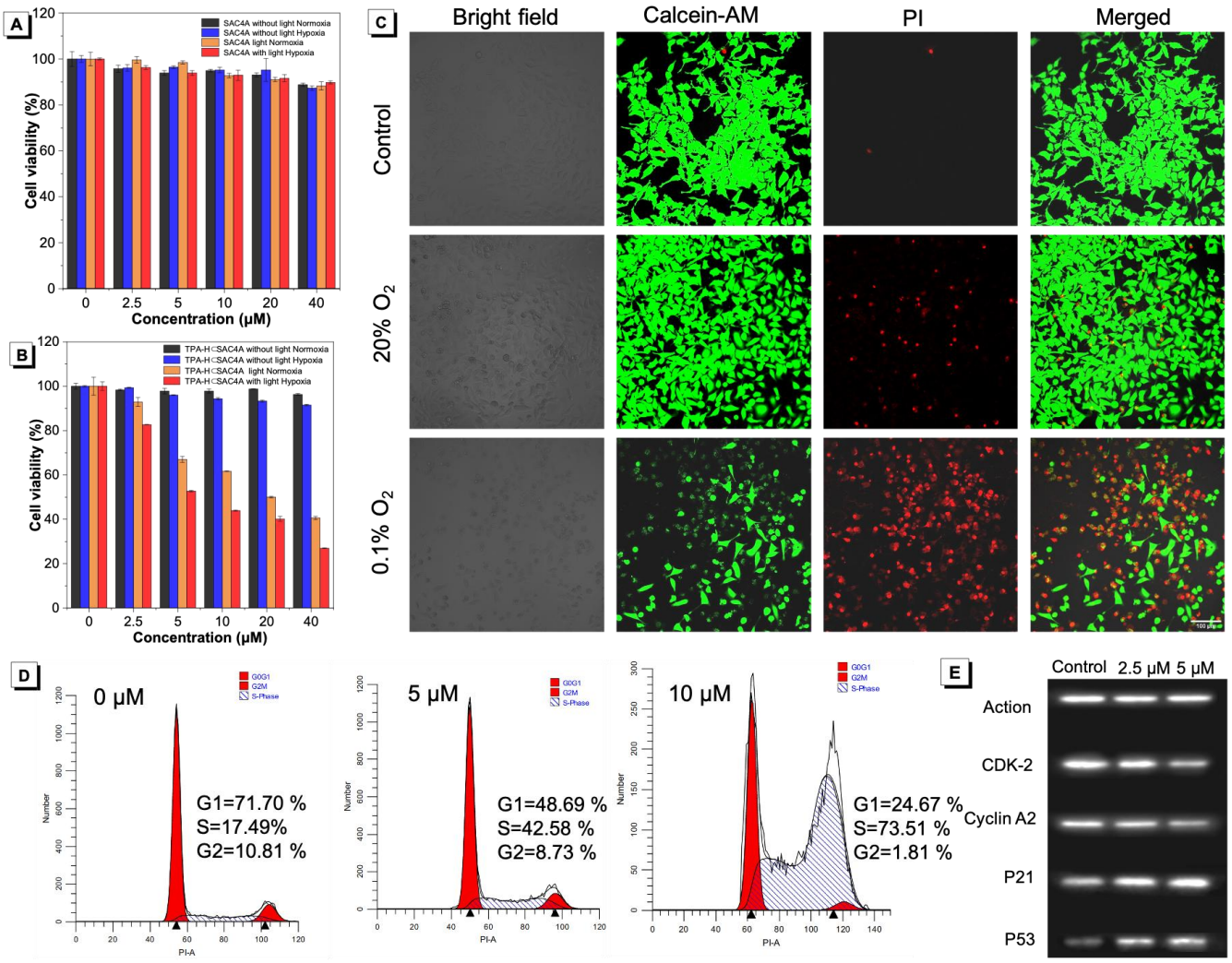

Figure 5. (A) Cell viabilities of HeLa cells treated with different concentrations of SAC4A under normoxic or hypoxic conditions without or with light. (B) Cell viabilities of HeLa cells treated with different concentrations of TPA-H⊂SAC4A under normoxic or hypoxic conditions without or with light. (C) Live/dead HeLa cell costaining assays using Calcein-AM and PI as fluorescence probes for TPA-H⊂SAC4A under different O_2 concentration with light irradiation. [TPA-H] = [SAC4A] = 40 μM. Calcein-AM: Ex = 488 nm, Em = 500–540 nm; PI: Ex = 561 nm, Em = 600–650 nm. (D) HeLa cells were treated with different concentrations (0, 5, 10 μM) of TPA-H, which were irradiated by white light for 30 min. The cell cycle was analyzed by flow cytometry. (E) HeLa cells were treated with different concentrations (0, 2.5, 5 μM) of TPA-H, which were irradiated by white light for 30 min. CDK-2, Cyclin A2, P21 and P53 protein expressions were detected by Western blot.

The good performance of TPA-H and TPA-H⊂SAC4A nanoparticles in cell experiments motivated us to further study in vivo hypoxia-responsive behaviors involving HeLa tumor-bearing BALB/c nude mice model. After intratumoral injection of TPA-H (100 μL, 1 mg mL^{-1}), the tumor site can be evidently observed strong fluorescence signals at 1 to 48 h, demonstrating its excellent tumor retention property (Figure 6A). In contrast, no fluorescence signals were detected at the initial stage after injection of TPA-H⊂SAC4A nanoparticles (Figure 6B). When prolonging the time to 12 h, obvious fluorescence was observed in the tumor site. This is because SAC4A was gradually decomposed in hypoxic tumors and released the included TPA-H to image the tumor tissues. Then, tumors and heart, liver, spleen, lung, kidney were collected to test their fluorescence intensities (Figure S26). Intense fluorescence signals were detected in tumor site, but almost no fluorescence signals were obtained in the main organs, which validated the prominent specificity and sustained tumor imaging ability.

The PDT treatment in vivo was carried out on 30 tumor-bearing BALB/c mice, and divided into 6 groups: PBS + light, SAC4A + light, TPA-H, TPA-H + light, TPA-H⊂SAC4A, TPA-H⊂SAC4A + light groups. After intratumoral injection

of PBS, TPA-H and TPA-H⊂SAC4A, the tumor sites of PBS + light, TPA-H + light, TPA-H⊂SAC4A + light groups were exposed under white light for 30 min, and other groups without light irradiation were served as a control. The tumor size in volume and body weight were monitored every 2 days during the treatment. As illustrated in Figure 6C and 6D, the mice in the group PBS + light, SAC4A + light, TPA-H, TPA-H⊂SAC4A, showed similar tumor growth trend, implying that PBS and SAC4A with light irradiation, TPA-H and TPA-H⊂SAC4A without light irradiation, had no antitumor activity. However, the group of TPA-H + light showed outstanding PDT efficacy. As a hypoxia-sensitive PDT model, TPA-H⊂SAC4A + light group also afforded good antitumor activity. The stable body weights of all mice indicated good biocompatibility of TPA-H and TPA-H⊂SAC4A (Figure 6E). Hematoxylin and eosin (H&E) staining of tumors and major organs were conducted in each group to explore systemic toxicity. As shown in Figure 6F, no obvious damage and inflammatory lesion were obtained in the heart, liver, spleen, lung and kidney, but TPA-H + light and TPA-H⊂SAC4A + light groups showed remarkable necrosis of the cell nucleus. Additionally, blood routine assays of above all groups were implemented after 14 days' treatment, and few variations of the hematological indexes were detected in Table S2, further illustrating excellent antitumor activity and low systematic toxicity.

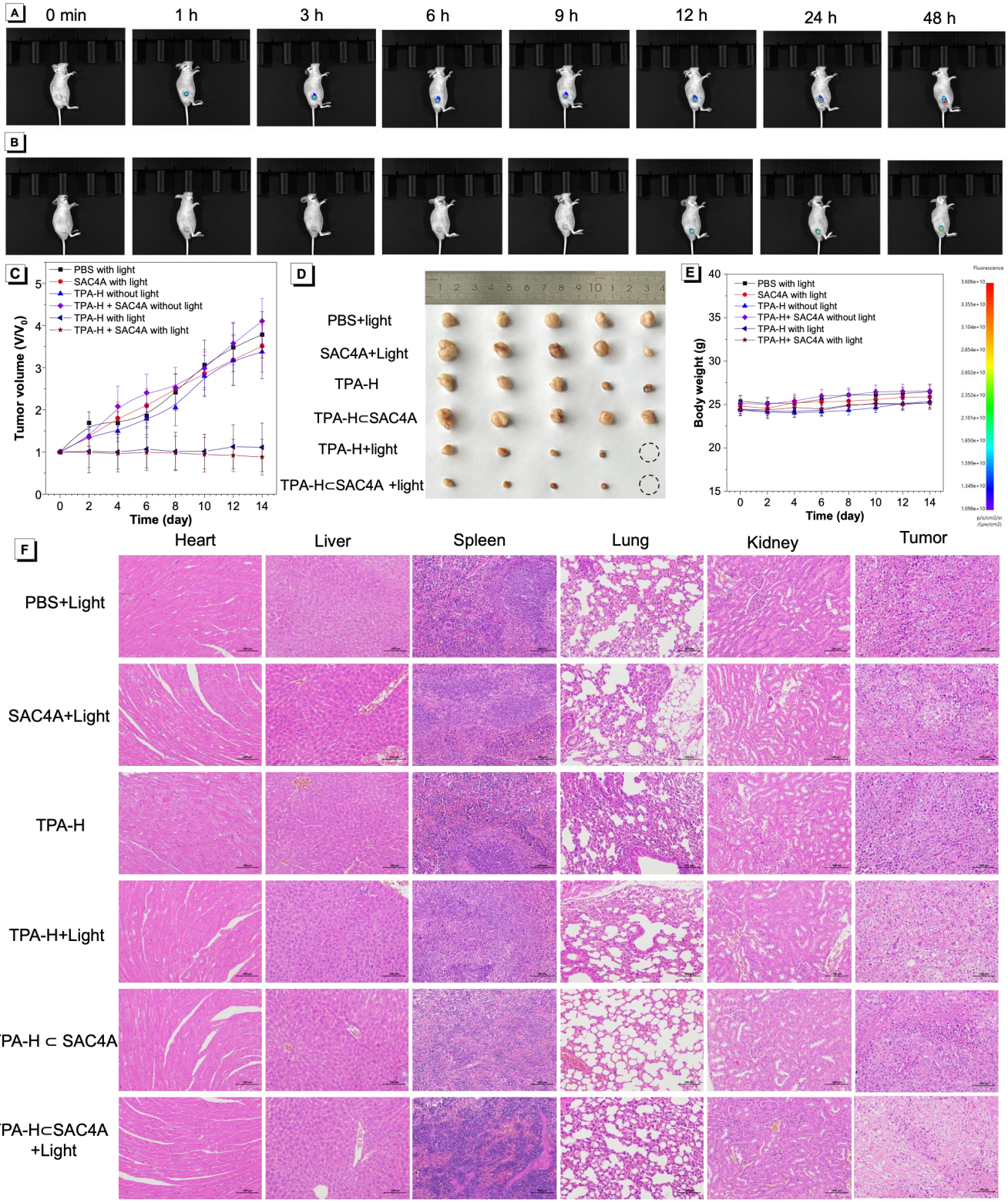

Figure 6. (A) Time-dependent in vivo images of HeLa tumor-bearing BALB/c nude mice in situ injected with TPA-H (A) and TPA-H ⊂ SAC4A (B). (C) The tumor volume changes during treatment process. (D) The corresponding tumor images in different treatment groups. (E) The body weight changes of tumor-bearing mice during treatment process. (F) H&E stained sections of various organs and tumor tissues. Scale bar = 100 nm.

CONCLUSION

In summary, a hypoxia-responsive supramolecular photodynamic therapy system was constructed based on a cationic AIEgen (TPA-H) and water-soluble azocalixarene (SAC4A). Upon supramolecular assembly of TPA-H and SAC4A through electrostatic interaction, the red fluorescence of TPA-H was quenched and its ROS generation was largely inhibited. In hypoxic tumors, the azo group of SAC4A can be reduced to aniline derivative and released the included TPA-H to recover pristine fluorescence and ROS. Cell imaging revealed that free TPA-H translocated from cell membrane to

mitochondria, achieving dual-organelle targeting and a real-time self-reporting system to monitor dynamic molecule migration *in situ*. In vivo hypoxia-responsive tumor imaging and therapy were performed to find this supramolecular complexes have good biosafety and efficient antitumor activity. This work presented a promising platform for the construction of hypoxia-responsive supramolecular photosensitizer system and it will enrich the biomedical study based on supramolecular strategy.

ASSOCIATED CONTENT

Supporting Information

The Supporting Information is available free of charge on the ACS Publications website.

Materials and Methods; Photophysical data and Imaging data (PDF)

AUTHOR INFORMATION

Corresponding Author

* haitaofeng907@163.com
* tangbenz@cuhk.edu.cn

Author Contributions

The manuscript was written through contributions of all authors. / All authors have given approval to the final version of the manuscript.

Notes

The authors declare no competing financial interest.

ACKNOWLEDGMENT

This work was supported by the National Natural Science Foundation of China (52173152 and 21805002), the Fund of the Rising Stars of Shaanxi Province (2021KJXX-48), Research Foundation of Education Department of Shaanxi Province (21JK0487), Young Talent Fund of University Association for Science and Technology in Shaanxi, China (20190610 and 20210606), Scientific and Technological Innovation Team of Shaanxi Province (2022TD-36). All animal experiments were performed under the protocols approved by the Animal Care and Use Committee (Gansu University Of Chinese Medicine) (Serial number: GZRSQ2024-131).

REFERENCES

(1) Castano, A. P.; Mroz, P.; Hamblin, M. R. Photodynamic therapy and anti-tumour immunity. *Nat. Rev. Cancer* **2006**, *6*, 535–545.

(2) Lucky, S. S.; Soo, K. C.; Zhang, Y. Nanoparticles in Photodynamic Therapy. *Chem. Rev.* **2015**, *115*, 1990–2042.

(3) Li, X.; Lovell, J. F.; Yoon, J.; Chen, X. Clinical development and potential of photothermal and photodynamic therapies for cancer. *Nat. Rev. Clin. Oncol.* **2020**, *17*, 657−674.

(4) Celli, J. P.; Spring, B. Q.; Rizvi, I.; Evans, C. L.; Samkoe, K. S.; Verma, S.; Pogue, B. W.; Hasan, T. Imaging and photodynamic therapy: Mechanisms, monitoring, and optimization. *Chem. Rev.* **2010**, *110*, 2795−2838.

(5) Pham, T. C.; Nguyen, V. N.; Choi, Y.; Lee, S.; Yoon, J. Recent strategies to develop innovative photosensitizers for enhanced photodynamic therapy. *Chem. Rev.* **2021**, *121*, 13454−13619.

(6) Zhou, Z.; Song, J.; Nie, L.; Chen, X. Reactive Oxygen Species Generating Systems Meeting Challenges of Photodynamic Cancer Therapy. *Chem. Soc. Rev.* **2016**, *45*, 6597−6626.

(7) Gottesman, M. M.; Fojo, T.; Bates, S. E. Multidrug Resistance in Cancer: Role of ATP−dependent Transporters. *Nat. Rev. Cancer* **2002**, *2,* 48−58.

(8) Dolmans, D. E.; Fukumura, D.; Jain, R. K. Photodynamic therapy for cancer. *Nat. Rev. Cancer* **2003**, *3,* 380−387.

(9) Samuel, E. L. G.; Marcano, D. C.; Berka, V.; Bitner, B. R.; Wu, G.; Potter, A.; Fabian, R. H.; Pautler, R. G.; Kent, T. A.; Tsai, A.-L.; Tour, J. M. Highly efficient conversion of superoxide to oxygen using hydrophilic carbon clusters. *Proc. Natl. Acad. Sci.* **2015**, *112*, 2343−2348.

(10) Chen, P.; Shan, G.; Nie, Q.; Yan, Y.; Zhang, P.; Zhao, Z.; Feng, H.-T.; Tang, B. Z. Two-color Emissive AIEgens with Anti-Kasha Property for Dual-Organelle Imaging and Phototherapy. *Sci. China Chem.* doi: 10.1007/s11426-015-5408-0.

(11) Tang, Y.; Pei, F.; Lu, X.; Fan, Q.; Huang, W. Recent Advances on Activatable NIR-II Fluorescence Probes for Biomedical Imaging. *Adv. Opt. Mater.* **2019**, *7*, 1900917.

(12) Tang, Y.; Wang, X.; Zhu, G.; Liu, Z.; Chen, X.-M.; Bisoyi, H. K.; Chen, X.; Chen, X.; Xu, Y.; Li, J.; Li, Q. Hypoxia-Responsive Photosensitizer Targeting Dual Organelles for Photodynamic Therapy of Tumors. *Small* **2023**, *19,* 2205440.

(13) Brown, J. M.; Wilson, W. R. Exploiting tumour hypoxia in cancer treatment. *Nat. Rev. Cancer* **2004,** *4,* 437–447.

(14) Gatenby, R. A.; Gillies, R. J. A microenvironmental model of carcinogenesis. *Nat. Rev. Cancer* **2008**, *8,* 56–61.

(15) Liu, J.-N.; Bu, W.; Shi, J. Chemical Design and Synthesis of Functionalized Probes for Imaging and Treating Tumor Hypoxia. *Chem. Rev.* **2017**, *117,* 6160−6224.

(16) Zhao, L.; Fu, C.; Tan, L.; Li, T.; Zhong, H.; Meng, X. Advanced Nanotechnology for Hypoxia-Associated Antitumor Therapy. *Nanoscale* **2020**, *12,* 2855−2874.

(17) Sundaram, A.; Peng, L.; Chai, L.; Xie, Z.; Ponraj, J. S.; Wang, X.; Wang, G.; Zhang, B.; Nie, G.; Xie, N.; Kumar, M. R.; Zhang, H. Advanced Nanomaterials for Hypoxia Tumor Therapy: Challenges and Solutions. *Nanoscale* **2020**, *12,* 21497−21518.

(18) Chen, H.; Wan, Y.; Cui, X.; Li, S.; Lee, C.-S. Recent Advances in Hypoxia-Overcoming Strategy of Aggregation-Induced Emission Photosensitizers for Efficient Photodynamic Therapy. *Adv. Healthcare Mater.* **2021**, *10*, 2101607.

(19) Thambi, T.; Park, J. H.; Lee, D. S. Hypoxia-Responsive Nanocarriers for Cancer Imaging and Therapy: Recent Approaches and Future Perspectives. *Chem. Commun.* **2016**, *52,* 8492−8500.

(20) Zhang, T.-X.; Zhang, Z.-Z.; Yue, Y.-X.; Hu, X.-Y.; Huang, F.; Shi, L.; Liu, Y.; Guo, D.-S. A General Hypoxia-Responsive Molecular Container for Tumor-Targeted Therapy. *Adv. Mater.* **2020**, *32,* 1908435.

(21) Chang, Q.; Jurisica, I.; Do, T.; Hedley, D. W. Hypoxia Predicts Aggressive Growth and Spontaneous Metastasis Formation from Orthotopically Grown Primary Xenografts of Human Pancreatic Cancer. *Cancer Res.* **2011**, *71,* 3110–3120.

(22) Teicher, B. A. Hypoxia and drug resistance. *Cancer Metastasis Rev*. **1994**, *13,* 139–168.

(23) Yang, S.; Tang, Z.; Hu, C.; Zhang, D.; Shen, N.; Yu, H.; Chen, X. Selectively Potentiating Hypoxia Levels by Combretastatin A4 Nanomedicine: Toward Highly Enhanced Hypoxia-Activated Prodrug Tirapazamine Therapy for Metastatic Tumors. *Adv. Mater.* **2019**, *31,* 1805955.

(24) Wang, H.; Xue, Ke.-F.; Yang, Y.; Hu, H.; Xu, J.-F.; Zhang, X. In Situ Hypoxia-Induced Supramolecular Perylene Diimide Radical Anions in Tumors for Photothermal Therapy with Improved Specificity. *J. Am. Chem. Soc.* **2022**, *144,* 2360−2367.

(25) Zhou, H.; Guo, M.; Li, J.; Qin, F.; Wang, Y.; Liu, T.; Liu, J.; Sabet, Z. F.; Wang, Y.; Liu, Y.; Huo, Q.; Chen, C. Hypoxia-Triggered Self-Assembly of Ultrasmall Iron Oxide Nanoparticles to Amplify the Imaging Signal of a Tumor. *J. Am. Chem. Soc.* **2021**, *143,* 1846−1853.

(26) Sharma, A.; Arambula, J. F.; Koo, S.; Kumar, R.; Singh, H.; Sessler, J. L.; Kim, J. S. Hypoxia-Targeted Drug Delivery. *Chem. Soc. Rev.* **2019**, *48,* 771−813.

(27) Takahashi, S.; Piao, W.; Matsumura, Y.; Komatsu, T.; Ueno, T.; Terai, T.; Kamachi, T.; Kohno, M.; Nagano, T.; Hanaoka, K. Reversible Off-On Fluorescence Probe for Hypoxia and Imaging of

Hypoxia-Normoxia Cycles in Live Cells. *J. Am. Chem. Soc.* **2012,** *134,* 19588−19591.

(28) Shi, Z.; Meng, X.; Zhang, K.; Tang, S.; Zhang, C.; Yang, Z.; Dong, H.; Zhang, X. Engineering Structural Metal−Organic Framework for Hypoxia-Tolerant Type I Photodynamic Therapy against Hypoxic Cancer. *ACS Materials Lett.* **2021**, *3,* 781−789.

(29) Zhao, X.-B.; Kang, J.-Y.; Shi, Y.-P. Noncovalent Dual-Locked Near-Infrared Fluorescent Probe for Precise Imaging of Tumor via Hypoxia/Glutathione Activation. *Anal. Chem.* **2022**, *94,* 6574−6581.

(30) Piao, W.; Tsuda, S.; Tanaka, Y.; Maeda, S.; Liu, F.; Takahashi, S.; Kushida, Y.; Komatsu, T.; Ueno, T.; Terai, T.; Nakazawa, T.; Uchiyama, M.; Morokuma, K.; Nagano, T.; Hanaoka, K. Development of Azo-Based Fluorescent Probes to Detect Different Levels of Hypoxia. *Angew. Chem. Int. Ed.* **2013**, *125,* 13266−13270.

(31) Wang, L.; Li, Q. Photochromism into nanosystems: towards lighting up the future nanoworld. *Chem. Soc. Rev.* **2018**, *47*, 1044−1097.

(32) Bandara, H. M. D.; Burdette, S. C. Photoisomerization in different classes of azobenzene. *Chem. Soc. Rev.* **2012**, *41,* 1809−1825.

(33) Kiyose, K.; Hanaoka, K.; Oushiki, D.; Nakamura, T.; Kajimura, M.; Suematsu, M.; Nishimatsu, H.; Yamane, T.; Terai, T.; Hirata, Y.; Nagano, T.; Hypoxia-Sensitive Fluorescent Probes for In Vivo Real-Time Fluorescence Imaging of Acute Ischemia. *J. Am. Chem. Soc.* **2010**, *132*, 15846–15848.

(34) Perche, F.; Biswas, S.; Wang, T.; Zhu, L.; Torchilin, V. P. Hypoxia-Targeted siRNA Delivery. *Angew. Chem. Int. Ed.* **2014**, *53,* 3362–3366.

(35) Yuan, P.; Zhang, H.; Qian, L.; Mao, X.; Du, S.; Yu, C.; Peng, B.; Yao, S. Q. Intracellular Delivery of Functional Native Antibodies under Hypoxic Conditions by Using a Biodegradable Silica Nanoquencher. *Angew. Chem. Int. Ed.* **2017**, 56, 12481–12485.

(36) Zhang, Z.; Wang, W.; O'Hagan, M.; Dai, J.; Zhang, J.; Tian, H. Stepping Out of the Blue: From Visible to Near-IR Triggered Photoswitches. *Angew. Chem. Int. Ed.* **2022**, *61*, e202205758.

(37) Hao, B.; Wang, J.; Wang, C.; Xue, K.; Xiao, M.; Lv, S.; Zhu, C. Bridging D–A type photosensitizer with the azo group to boost intersystem crossing for efficient photodynamic therapy. *Chem. Sci.* **2022**,*13*, 4139−4149.

(38) Samanta, S.; Beharry, A. A.; Sadovski, O.; McCormick, T. M. Photoswitching Azo Compounds in Vivo with Red Light. *J. Am. Chem. Soc.* **2013**, *135*, 9777–9784.

(39) Piao, W.; Tsuda, S.; Tanaka, Y.; Maeda, S.; Liu, F.; Takahashi, S.; Kushida, Y.; Komatsu, T.; Ueno, T.; Terai, T.; Nakazawa, T.; Uchiyama, M.; Morokuma, K.; Nagano, T.; Hanaoka, Kenjiro. Development of Azo-Based Fluorescent Probes to Detect Different Levels of Hypoxia. *Angew. Chem. Int. Ed.* **2013**, *52,* 13028−13032.

(40) Dai, J.; Duan, C.; Huang, Y.; Lou, X.; Xia, F.; Wang, S. Aggregation-induced emission luminogens for RONS sensing. *J. Mater. Chem. B* **2020**, *8,* 3357−3370.

(41) Luo, J.; Xie, Z.; Lam, J. W. Y.; Cheng, L.; Chen, H.; Qiu, C.; Kwok, H. S.; Zhan, X.; Liu, Y.; Zhu, D.; Tang, B. Z. Aggregation-induced emission of 1-methyl-1,2,3,4,5-pentaphenylsilole. *Chem. Commun.* **2001**, 1740−1741.

(42) Yuan, Y. Y.; Zhang, C.-J.; Gao, M.; Zhang, R. Y.; Tang, B. Z.; Liu, B. Specific Light-up Bioprobe with Aggregation-Induced Emission and Activatable Photoactivity for Targeted and Image-Guided Photodynamic Ablation of Cancer Cells. *Angew. Chem. Int. Ed.* **2015**, *54*, 1780−1786.

(43) Ye, Z.; He, W.; Zhang, Z.; Qiu, Z.; Zhao, Z.; Tang, B. Z. AIEgens for microorganism-related visualization and therapy. *Interdiscip. Med.* **2023**, *1*, e20220011.

(44) Wang, X.; Chen, P.; Yang, H.; Liu, J.; Tu, R.; Feng, H.-T.; Dai, H. In Situ Imaging and Anti-inflammation of 3D Printed Scaffolds Enabled by AIEgen. *ACS Appl. Mater. Interfaces* **2023**, *15*, 25382−25392.

(45) Qi, C.; Wei, K.; Li, Q.; Li, Y.; Su, X.; Yang, J.-C.; Tian, J.; Chen, P.; Feng, H.-T.; Tang, B. Z. Visualization of enantioselective recognition and separation of chiral acids by aggregation-induced emission chiral diamine. *Aggregate* **2023**, *4*, e299.

(46) Wang, X.; Xiang, S.; Qi, C.; Chen, M.; Su, X.; Yang, J.-C.; Tian, J.; Feng, H.-T.; Tang, B. Z. Visualization of Enantiorecognition and Resolution by Chiral AIEgens. *ACS Nano* **2022**, *16*, 8223–8232.

(47) Feng, H.-T.; Zou, S.; Chen, M.; Xiong, F.; Lee, M.-H.; Fang, L.; Tang, B. Z. Tuning Push–Pull Electronic Effects of AIEgens to Boost the Theranostic Efficacy for Colon Cancer. *J. Am. Chem. Soc.* **2020**, *142*, 11442–11450.

(48) Yuan, Y.; Zhang, C.-J.; Xu, S.; Liu, B. A self-reporting AIE probe with a built-in singlet oxygen sensor for targeted photodynamic ablation of cancer cells. *Chem. Sci.* **2016**, *7*, 1862−1866.

(49) Gao, M.; Tang, B. Z. AIE-based cancer theranostics. *Coord. Chem. Rev.* **2020**, *402*, 213076.

(50) Yu, G.; Jie, K.; Huang, F. Supramolecular amphiphiles based on host−guest molecular recognition motifs. *Chem. Rev.* **2015**, *115*, 7240−7303.

(51) Feng, H.-T.; Yuan, Y.-X.; Xiong, J.-B.; Zheng, Y.-S.; Tang, B. Z. Macrocycles and cages based on tetraphenylethylene with aggregation-induced emission effect. *Chem. Soc. Rev.* **2018**, *47*, 7452-7476.

(52) Feng, H.-T.; Lam, J. W. Y.; Tang, B. Z. Self-assembly of AIEgens. *Coord. Chem. Rev.* **2020**, *406*, 213142.

(53) Shao, L.; Pan, Y.; Hua, B.; Xu, S.; Yu, G.; Wang, M.; Liu, B.; Huang, F. Constructing Adaptive Photosensitizers via Supramolecular Modification Based on Pillararene Host−Guest Interactions. *Angew. Chem. Int. Ed.* **2020**, *59*, 11779−11783.

(54) Li, J.; Wang, J.; Li, H.; Song, N.; Wang, D.; Tang, B. Z. Supramolecular materials based on AIE luminogens (AIEgens): construction and applications. *Chem. Soc. Rev.* **2020**, *49*, 1144−1172.

(55) Dsouza, R. N.; Pischel, U.; Nau, W. M. Fluorescent dyes and their supramolecular host/guest complexes with macrocycles in aqueous solution. *Chem. Rev.* **2011**, *111*, 7941−7980.

(56) Guo, D.-S.; Liu, Y. Supramolecular Chemistry of p-Sulfonatocalix[n]arenes and Its Biological Applications. *Acc. Chem. Res.* **2014**, *47*, 1925–1934.

(57) Hu, X.-Y.; Chen, Y.; Liu, Y. Redox-responsive supramolecular nanoparticles based on amphiphilic sulfonatocalixarene and selenocystamine dihydrochloride. *Chin Chem Lett* **2015***, 26,* 862–866.

(58) Wang, R.-P.; Liu, W.; Wang, X.; Shan, G.; Liu, T.; Xu, F.; Dai, H.; Qi, C.; Feng, H.-T.; Tang, B. Z. Supramolecular Assembly Based on Calix(4)arene and Aggregation-Induced Emission Photosensitizer for Phototherapy of Drug-Resistant Bacteria and Skin Flap Transplantation. *Adv. Healthcare Mater.* **2024**, 2303336.

(59) Chen, C.; Ni, X.; Tian, H.-W.; Liu, Q.; Guo, D.-S.; Ding, D. Calixarene-Based Supramolecular AIE Dots with Highly Inhibited Nonradiative Decay and Intersystem Crossing for Ultrasensitive Fluorescence Image-Guided Cancer Surgery. *Angew. Chem. Int. Ed.* **2020**, *59*, 10008−10012.

(60) Liu, Z.; Dai, X.; Sun, Y.; Liu, Y. Organic supramolecular aggregates based on water-soluble cyclodextrins and calixarenes. *Aggregate* **2020**, *1*, 31–44.

(61) Yao, S.-Y.; Yue, Y.-X.; Ying, A.-K. Hu, X.-Y. Li, H.-B.; Cai, K.; Guo, D.-S. An Antitumor Dual-Responsive Host-Guest Supramolecular Polymer Based on Hypoxia-Cleavable Azocalix[4]arene. *Angew. Chem. Int. Ed.* **2020**, *59*, 10008−10012.

(62) Geng, W.-C.; Jia, S.; Zheng, Z.; Li, Z.; Ding, D. Guo, D.-S. A Noncovalent Fluorescence Turn-on Strategy for Hypoxia Imaging. *Angew. Chem. Int. Ed.* **2019**, *131*, 1–6.

(63) Geng, W.-C.; Ye, Z.; Zheng, Z.; Gao, J.; Li, J.-J.; Shah, M. R.; Xiao, L.; Guo, D.-S. Supramolecular Bioimaging through Signal Amplification by Combining Indicator Displacement Assay with Forster Resonance Energy Transfer. *Angew. Chem. Int. Ed.* **2021**, *60*, 1–7.

SYNOPSIS TOC: A supramolecular assembly strategy based on sulfonate-functionalized azocalix[4]arene and cationic aggregation-induced emission photosensitizer was proposed for hypoxia-responsive bioimaging and photodynamic therapy.